

Diffusion-Based Synthesis of 3D T1w MPRAGE Images from Multi-Echo GRE with Multi-Parametric MRI Integration

Sizhe Fang*

Deqiang Qiu[†]

November 2025

Abstract

Multi-echo Gradient Echo (mGRE) sequences provide valuable quantitative parametric maps, such as Quantitative Susceptibility Mapping (QSM) and transverse relaxation rate ($R2^*$), which are sensitive to tissue iron and myelin. However, structural morphometry typically relies on separate T1-weighted MPRAGE acquisitions, prolonging scan times. We propose a deep learning framework to synthesize high-contrast 3D T1w MPRAGE images directly from mGRE data, thereby streamlining neuroimaging protocols. We developed a novel multi-parametric conditional diffusion model based on the Fast-DDPM architecture. Unlike conventional intensity-based synthesis, our approach integrates iron-sensitive QSM and $R2^*$ maps as physical priors to address the challenge of contrast ambiguity in iron-rich deep gray matter structures. We trained and validated the model on a cohort of 175 healthy subjects. Performance was evaluated against established U-Net and GAN-based baselines using perceptual metrics and downstream segmentation accuracy. Uniquely, we assessed the biological plausibility of the synthesized images by replicating population-level statistical associations with age and sex. The proposed framework significantly outperformed baseline methods, achieving superior perceptual quality and segmentation accuracy, particularly in subcortical regions like the thalamus and pallidum. Crucially, the synthesized images preserved essential biological dependencies: regression analyses demonstrated high concordance in age-related atrophy rates, aging effect sizes, and sexual dimorphism patterns compared to ground truth data. By effectively leveraging quantitative MRI priors, our diffusion-based method generates strictly biologically plausible T1w images suitable for reliable clinical morphometric analysis. This approach offers a promising pathway to reduce acquisition time by deriving structural contrasts retrospectively from quantitative mGRE sequences.

Keywords: MRI Synthesis, Denoising Diffusion Probabilistic Models, Multi-Echo GRE, Quantitative Susceptibility Mapping (QSM), Deep Learning, Neuroimaging.

1 Introduction

Magnetic Resonance Imaging (MRI) provides essential anatomical and functional information for clinical diagnosis and neuroimaging research through diverse imaging sequences. T1-weighted Magnetization Prepared Rapid Gradient Echo (T1w MPRAGE) images are widely acquired in neuroimaging studies due to their superior gray matter-white matter contrast, making them essential for brain morphometry and tissue segmentation [1, 2]. Multi-echo Gradient Echo (mGRE) sequences, on the other hand, enable quantitative parametric mapping including transverse relaxation rate ($R2^*$) and quantitative susceptibility mapping (QSM),

*Department of Radiology and Imaging Sciences, Emory University, Atlanta, GA, USA. School of Biological Sciences, Georgia Institute of Technology, Atlanta, GA, USA. Email: sfang86@gatech.edu

[†]Corresponding author. Department of Radiology and Imaging Sciences, Emory University, Atlanta, GA, USA. Email: dqiu3@emory.edu

which are highly sensitive to iron deposition and myelin content in brain tissue [3, 4]. In typical neuroimaging protocols, both sequences are acquired to provide complementary structural and quantitative information. However, this results in prolonged scan times, increasing patient burden and scanning costs. The ability to synthesize MPRAGE images from mGRE data could streamline imaging workflows while maintaining access to both structural morphometry and quantitative parametric maps.

Medical image synthesis using deep learning has shown promise in addressing the limitations of multi-sequence acquisition protocols [5, 6]. Early approaches relied on traditional machine learning methods such as atlas-based techniques and random forests, which suffered from limited generalizability and often required manual intervention [7, 8]. The advent of deep learning brought significant advances, with convolutional neural networks (CNNs) and U-Net architectures demonstrating success in various cross-modality synthesis tasks [9, 10]. Generative Adversarial Networks (GANs) further improved synthesis quality through adversarial training, becoming widely adopted for medical image generation [11, 12]. However, GANs can suffer from training instability and mode collapse, which may compromise the reliability of synthesized medical images [13].

Recently, denoising diffusion probabilistic models (DDPMs), or diffusion models, have emerged as a powerful alternative for medical image synthesis. Unlike GANs that rely on adversarial training, diffusion models generate images through an iterative denoising process, offering superior stability and sample quality [14, 15]. Recent medical imaging applications have demonstrated their effectiveness in cross-modality MRI synthesis and image reconstruction [16, 17]. Notably, the Fast-DDPM framework has made diffusion models more practical by reducing sampling steps from 1,000 to 10 while maintaining generation quality [18].

For quantitative neuroimaging studies using mGRE images, MPRAGE acquisitions serve a critical role by providing anatomical references for tissue segmentation and region-based analysis of QSM and $R2^*$ maps. QSM quantifies magnetic susceptibility distributions within tissues and has shown particular value in detecting iron accumulation in deep gray matter structures, which is a biomarker relevant to aging and neurodegenerative diseases [19, 20]. $R2^*$ mapping similarly reflects tissue microstructural properties influenced by iron content and field inhomogeneities [21]. While automated segmentation tools like FreeSurfer require high-quality T1-weighted images for accurate parcellation, acquiring separate MPRAGE scans adds 5-6 minutes to imaging protocols. Ryu et al. previously demonstrated the feasibility of synthesizing MPRAGE from mGRE using a 3D U-Net, achieving good segmentation accuracy and correlation for susceptibility measurements [22]. However, intensity-based approaches may struggle to resolve contrast ambiguity in iron-rich deep gray matter structures. Building upon this foundation, recent advances in generative modeling and the availability of derived parametric maps from mGRE data motivate further exploration of this synthesis task.

In this study, we investigate the application of conditional diffusion models for synthesizing T1w MPRAGE images from mGRE data with multi-parametric MRI integration. Specifically, we adapt the Fast-DDPM framework and explore whether incorporating derived QSM and $R2^*$ maps alongside mGRE magnitude images can enhance synthesis quality. We systematically evaluate our approach through both qualitative and quantitative methods. Comparative experiments with U-Net and GAN baselines assess the relative advantages of the diffusion-based approach. Finally, we demonstrate the practical utility of synthesized MPRAGE images by applying them to investigate age-related brain structural changes. This work represents the first application of diffusion models to mGRE-to-MPRAGE synthesis and provides insights into multi-parametric conditioning strategies for cross-contrast MRI synthesis.

2 Materials and Method

2.1 Subjects

This study included 175 participants from the Emory Brain Imaging Program. The cohort comprised 129 females (mean age \pm SD = 54.49 \pm 18.46 years) and 46 males (mean age \pm SD = 48.85 \pm 20.40 years), with an

overall mean age of 53.0 ± 19.1 years. All participants provided written informed consent in accordance with a protocol approved by the Institutional Review Board of Emory University. All participants were cognitively normal individuals. Subjects with a prior history of neurological or psychiatric disorders were excluded from this study.

2.2 MRI Acquisition

All MRI scans were performed on a Siemens Magnetom Prisma 3T scanner equipped with a 32-channel phased-array head coil at the Brain Health Center of Emory University. A multi-echo 3D spoiled gradient echo (mGRE) sequence was acquired with the following parameters: voxel size = $0.72 \times 0.72 \times 1.44 \text{ mm}^3$, repetition time (TR) = 37 ms, five echoes with echo times (TE) = 6.61, 12.85, 19.09, 25.33, and 31.57 ms, and flip angle (FA) = 15° . Three-dimensional T1-weighted (T1w) images were acquired using a magnetization-prepared rapid gradient-echo (MPRAGE) sequence with the following parameters: TR = 2300 ms, TE = 2.96 ms, inversion time (TI) = 900 ms, FA = 9° , 208 sagittal slices with 1 mm slice thickness, in-plane matrix size = 256×240 , and isotropic voxel resolution of $1 \times 1 \times 1 \text{ mm}^3$.

2.3 Data Pre-Processing

QSM images were reconstructed from the mGRE data using an in-house processing pipeline[23], which included phase unwrapping, background field removal, and magnetic field-to-susceptibility inversion. $R2^*$ maps were calculated by performing monoexponential fitting to the magnitude signals across the five echoes of the mGRE sequence (FA = 15°). Detailed descriptions of the QSM and $R2^*$ reconstruction procedures have been reported in our previous publications[24, 25]. T1w MPRAGE images were padded and cropped to a final matrix size of $256 \times 256 \times 160$ voxels. The first echo of the mGRE sequence was rigidly registered to the 1 mm isotropic MPRAGE images using the FLIRT toolbox[26] within FSL (FMRIB Software Library, Oxford, UK), and the resulting transformation matrix was applied to register the QSM and $R2^*$ maps to the MPRAGE space.

Following registration, all images were independently normalized to a range of -1 to 1 for each modality group. A brain mask extracted from the registered mGRE images was applied to remove extracerebral tissues from the T1w MPRAGE images. Given that brain iron is predominantly concentrated in basal ganglia and other deep gray matter structures[27, 28, 29], anatomical masks derived from the MNI152 standard template (registered to individual MPRAGE space) were applied to the QSM and $R2^*$ maps to extract five bilateral regions of interest: Caudate, Putamen, Pallidus, Accumbens, and Thalamus. To ensure complete coverage of these structures, the masks were dilated by 3 voxels. All voxels outside the masked regions were set to background values (-1 for QSM). Finally, each 3D volume was converted into 2D axial slices with dimensions of 256×256 pixels to accommodate the input format of the diffusion model.

2.4 Model Implement and Training Details

The dataset was partitioned into a training set ($n = 77$; 56 females, 21 males; mean age = 53.22 ± 19.13 years) and a test set ($n = 98$; 73 females, 25 males; mean age = 52.84 ± 19.17 years). No significant differences were observed between the two sets in terms of sex distribution ($p = 0.928$) or age ($p = 0.896$).

We implemented a conditional diffusion model based on the Fast-DDPM framework [18] to synthesize T1w MPRAGE images from multi-echo GRE images. The overall architecture is illustrated in Fig 1. The network consists of an encoder-decoder structure with skip connections. To accommodate multi-channel inputs, the initial convolutional layer was modified to accept $N+1$ channels, where N represents the number of input modalities and the additional channel corresponds to the noisy target during forward diffusion. Two

model configurations were trained: the first used five mGRE magnitude images as input (N=5), while the second incorporated QSM and R2* maps in addition to the five mGRE images (N=7).

The encoder employs convolutional blocks with a base channel dimension of 128 and channel multipliers of [1, 1, 2, 2, 4, 4]. Each level contains two residual blocks with group normalization (32 groups) and Swish activation. Self-attention layers are applied at the 16×16 resolution to capture long-range spatial dependencies. The decoder mirrors the encoder structure with transposed convolutions for upsampling. Skip connections transfer features from encoder to decoder at corresponding resolution levels.

Following the Fast-DDPM methodology, we reduced the number of diffusion timesteps from 1000 to 100. The forward diffusion process employs a linear- β noise schedule with $\beta_1 = 0.0001$ and $\beta_T = 0.02$ defined over 1000 virtual timesteps. During both training and inference, 100 timesteps were uniformly sampled from this schedule at intervals of 10 (i.e., timesteps 1, 11, 21, ..., 991). This approach enables the model to focus its learning on the most informative noise levels rather than uniformly distributing capacity across all possible diffusion stages. The training objective minimizes the mean squared error between predicted and ground truth noise:

$$\mathcal{L} = \mathbb{E}_{t, x_0, \varepsilon, c} \left[\left\| \varepsilon - \varepsilon_\theta \left(\sqrt{\bar{\alpha}_t} x_0 + \sqrt{1 - \bar{\alpha}_t} \varepsilon, c, t \right) \right\|^2 \right]$$

where ε_θ is the noise prediction network, x_0 is the ground truth T1w image, c represents the multi-channel input conditions, t is uniformly sampled from the 100 selected timesteps, $\varepsilon \sim \mathcal{N}(0, I)$ is Gaussian noise, and $\bar{\alpha}_t = \prod_{i=1}^t (1 - \beta_i)$.

The network was optimized using Adam [30] with learning rate 2×10^{-5} , $\beta_1 = 0.9$, $\beta_2 = 0.999$, and batch size 16 for 1,400,000 iterations. Antithetic sampling was employed for timestep selection, where for each batch, half of the samples used timestep index i and the other half used the complementary index from the opposite end of the timestep sequence. An exponential moving average (EMA) of model weights was maintained with decay rate 0.999. Model checkpoints were saved every 50,000 iterations. Training was performed on 4 NVIDIA A40 GPUs.

During inference, synthetic T1w MPRAGE images were generated using the generalized denoising procedure with deterministic sampling ($\eta = 0$). Starting from Gaussian noise $x_T \sim \mathcal{N}(0, I)$, the reverse diffusion process iteratively denoises the latent representation conditioned on the input images over the same 100 uniformly sampled timesteps used during training. The EMA model weights were used for all evaluations. The proposed method was compared against U-Net [9] and Pix2Pix [12] baselines trained on the same dataset.

2.5 Evaluation Metrics

2.5.1 Image Quality Assessment

In addition to qualitative analysis, to quantitatively evaluate the quality of synthesized T1w MPRAGE images, we employed two widely used metrics: peak signal-to-noise ratio (PSNR) and structural similarity index measure (SSIM)[31]. PSNR measures the pixel-wise fidelity between the synthesized and ground truth images, defined as:

$$\text{PSNR} = 10 \cdot \log_{10} \left(\frac{\text{MAX}_I^2}{\text{MSE}} \right)$$

where MAX_I represents the maximum possible pixel value and $\text{MSE} = \frac{1}{N} \sum_{i=1}^N (I_i - \hat{I}_i)^2$ is the mean squared error between the ground truth image I and synthesized image \hat{I} over N pixels.

SSIM evaluates the structural similarity between two images by comparing luminance, contrast, and structure, computed as:

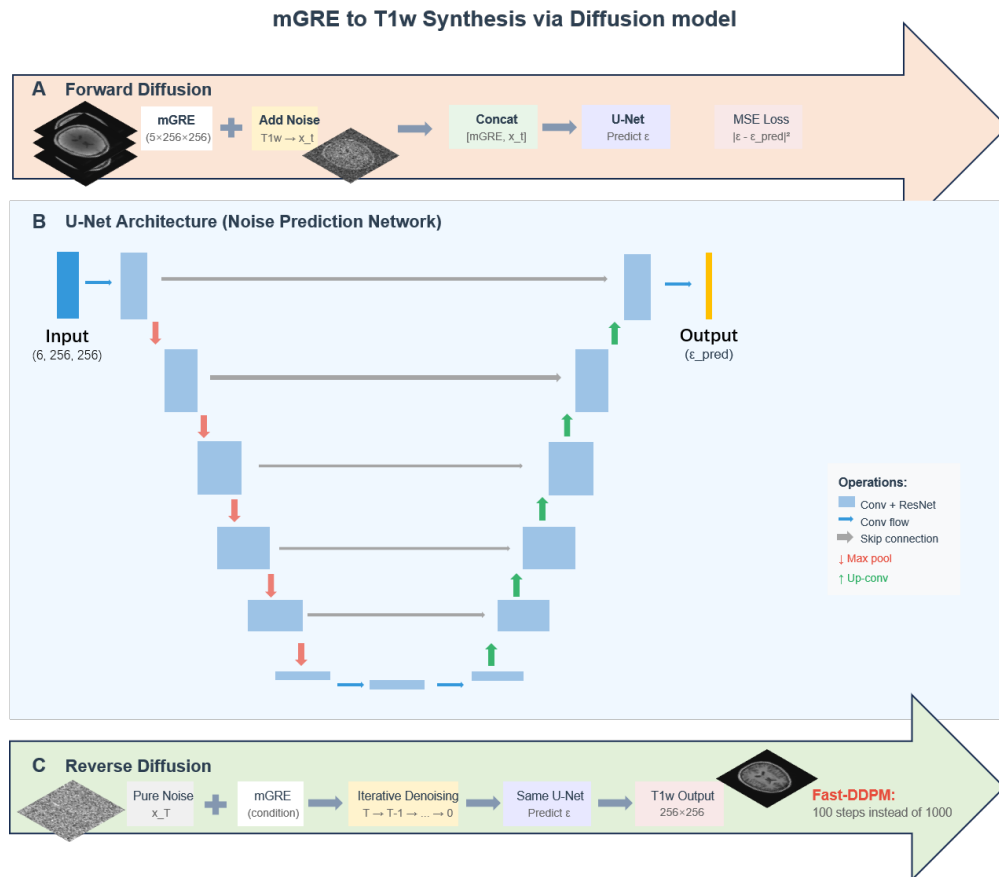


Figure 1: Architecture of the diffusion model for multi-echo gradient echo (mGRE) to T1-weighted image synthesis (2D slice as input). (A) Forward diffusion process: During training, Gaussian noise is progressively added to the T1w target image. The U-Net learns to predict the noise at each timestep. (B) U-Net noise prediction network: A standard encoder-decoder architecture that takes as input a 6-channel image (5-channel mGRE + 1-channel noisy image) or 8-channel image (6-channel image + 1-channel QSM + 1-channel R2*) and outputs a 1-channel predicted noise map. (C) Reverse diffusion process: During inference, the model starts from pure noise and iteratively denoises it under mGRE guidance to generate the T1w image. Fast-DDPM[18] is used to accelerate sampling compared to standard DDPM.

$$\text{SSIM}(I, \hat{I}) = \frac{(2\mu_I\mu_{\hat{I}} + C_1)(2\sigma_{I\hat{I}} + C_2)}{(\mu_I^2 + \mu_{\hat{I}}^2 + C_1)(\sigma_I^2 + \sigma_{\hat{I}}^2 + C_2)}$$

where μ_I and $\mu_{\hat{I}}$ are the mean intensities, σ_I^2 and $\sigma_{\hat{I}}^2$ are the variances, $\sigma_{I\hat{I}}$ is the covariance, and C_1, C_2 are stabilization constants.

2.5.2 Segmentation-Based Functional Assessment

Since T1w MPRAGE images are primarily acquired for anatomical segmentation rather than quantitative analysis, we evaluated the functional utility of synthesized images by comparing tissue segmentation performance. Both synthesized and ground truth MPRAGE images were automatically segmented using FreeSurfer [2] without manual intervention. Segmentation accuracy was quantified using the Dice similarity coefficient (DSC) [32]:

$$\text{DSC}(G, S) = \frac{2|G \cap S|}{|G| + |S|}$$

where S represents the binary segmentation from synthesized MPRAGE and G represents the segmentation from ground truth MPRAGE. DSC values range from 0 to 1, with higher values indicating better spatial overlap. We calculated DSC for eight representative brain regions: cortex, cerebral white matter, putamen, pallidum, thalamus, caudate, amygdala, and hippocampus. For bilateral structures, left and right hemispheres were analyzed separately and then averaged. Statistical significance of differences between methods was assessed using paired t-tests.

To quantify the reliability of volumetric measurements across different segmentation models, we computed the intraclass correlation coefficient (ICC) with two-way mixed effects model (ICC2k) [33] for the eight brain regions. ICC values above 0.75 indicate good reliability [34].

2.5.3 Baseline Comparisons

For comparison, we trained two baseline methods using the same generator architecture: (1) supervised learning with L1 loss (U-Net baseline), and (2) Pix2Pix [12] with combined L1 and adversarial losses. All methods were trained on the same dataset to ensure fair comparison.

2.5.4 Biological Plausibility Assessment

To assess whether synthesized images preserve biologically meaningful information for clinical research on aging effects, we performed regression analyses on brain regional volumes and cortical thickness. We compared the best-performing generative model against ground truth using age and sex as covariates.

Independent multiple linear regression (MLR) analyses were conducted on nine regions of interest (ROIs) to evaluate whether synthesized data (D_{GEN}) could replicate the established associations between brain morphology and demographic variables observed in ground truth data (D_{GT}). For each ROI, the regression model was formulated as:

$$Y_{\text{ROI}} = \beta_0 + \beta_{\text{Age}} \cdot \text{Age} + \beta_{\text{Sex}} \cdot \text{Sex} + \beta_{\text{eTIV}} \cdot \text{eTIV} + \epsilon$$

where Y_{ROI} represents regional volume or mean cortical thickness (cortical thickness measures are not influenced by head size; therefore, correction for eTIV is not required), and ϵ is the error term. Age and sex were included as independent variables. Estimated total intracranial volume (eTIV) was included as a covariate for volumetric analyses to correct for head size but excluded from cortical thickness models [35].

The aging effect was quantified using the regression coefficient β_{Age} , which indicates the annual rate of change in the regional measure, along with its corresponding p -value. Furthermore, we calculated Cohen’s f to evaluate the effect size of aging, derived as the square root of Cohen’s f^2 [36]. To evaluate the fidelity of generated data, we compared these derived metrics (adjusted R^2 , β_{Age} , Cohen’s f for aging effect, and Cohen’s d for sex differences) between D_{GEN} and D_{GT} groups. High alignment between coefficients would indicate that the generative model successfully preserves the biological dependencies present in the real population.

3 Results

3.1 Image Synthesis Performance

We evaluated the image synthesis quality of the proposed diffusion model against two baseline methods (U-Net and Pix2Pix) using both quantitative metrics and qualitative visual assessment. For quantitative evaluation, slices containing only background (identical to ground truth) were excluded from metric calculations to avoid bias.

Quantitative Analysis. Table 1 presents the quantitative comparison results across four model configurations. Both PSNR and SSIM metrics demonstrate that the diffusion-based models substantially outperform the baseline methods. Specifically, the proposed diffusion model achieved improvements of up to 1.75 dB in PSNR and 0.0270 in SSIM compared to baselines. Between the two diffusion model variants, incorporating QSM and R2* maps as additional input modalities yielded nearly identical performance (PSNR: 29.20 vs 29.23 dB; SSIM: 0.8883 vs 0.8891), suggesting that the quantitative image similarity metrics alone may not fully capture the biological information preserved by these additional parametric maps. Both diffusion models demonstrated high fidelity to the ground truth MPRAGE images, with PSNR values exceeding 29 dB and SSIM scores approaching 0.89.

Table 1: Quantitative comparison of image synthesis performance across different models. Metrics are reported as Mean \pm Standard Deviation over the test set ($n = 98$ subjects). PSNR is measured in decibels (dB), and SSIM ranges from 0 to 1, with higher values indicating better performance.

Model	PSNR (dB)	SSIM
U-Net	28.56 \pm 2.36	0.8754 \pm 0.0322
Pix2Pix	27.48 \pm 2.25	0.8621 \pm 0.0344
Diffusion (Ours)	29.23 \pm 2.39	0.8891 \pm 0.0341
Diffusion w/ QSM R2* (Ours)	29.20 \pm 2.39	0.8883 \pm 0.0340

Qualitative Analysis. Figure 2 provides a qualitative comparison of synthesized images across all methods for a representative test subject. Visual inspection reveals notable differences in image quality and structural fidelity. The baseline methods (U-Net and Pix2Pix) produced images with reduced sharpness and smoothed textures, particularly evident in the magnified basal ganglia region (middle row), where fine structural details and tissue boundaries appear blurred. This loss of anatomical detail is clinically significant, as precise delineation of brain structures is critical for accurate volumetric analysis and disease characterization. In contrast, both diffusion models generated images with sharper structural boundaries and better-preserved fine details. The absolute error maps (bottom row) demonstrate that the diffusion model with QSM and R2* inputs exhibits slightly reduced errors in deep gray matter regions, though the overall difference between the two diffusion variants remains subtle. Both diffusion models show substantially lower reconstruction errors compared to the baseline methods, as evidenced by the predominantly blue-green coloration in their error maps versus the more prominent red regions in the baseline error maps.

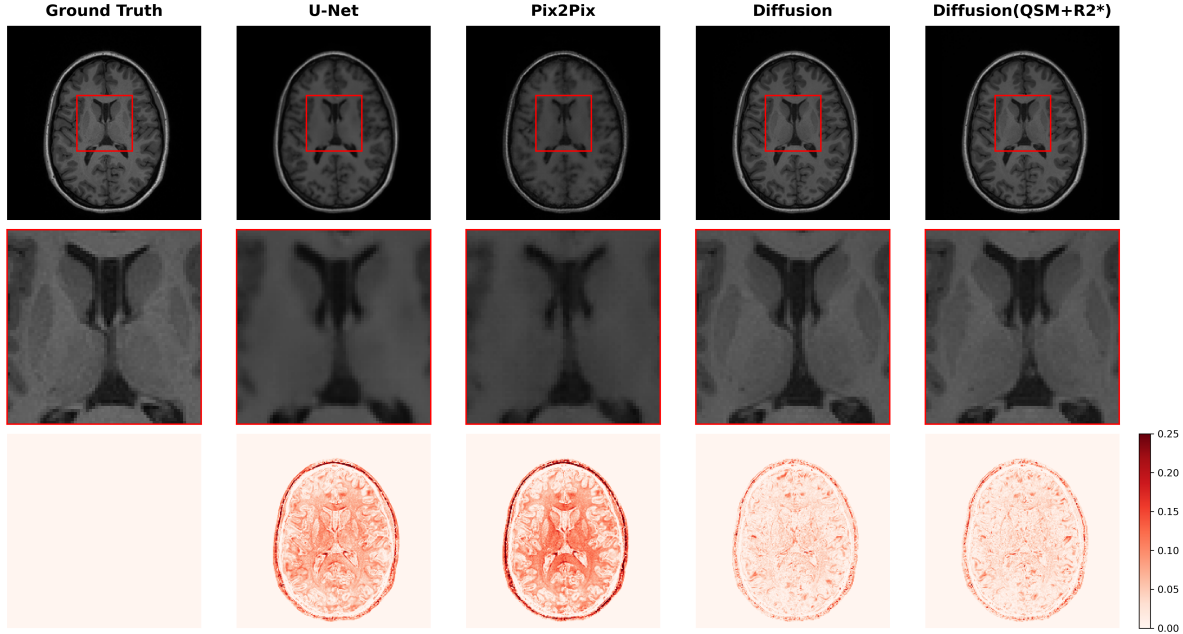


Figure 2: Qualitative comparison of synthesized T1-weighted MPRAGE images across different methods. From left to right: ground truth, U-Net, Pix2Pix, diffusion model, and diffusion model with QSM and R2* inputs. Top row: full axial slice; middle row: magnified view of the basal ganglia region (red box) showing structural details and tissue contrast; bottom row: absolute error maps relative to ground truth. The color bar indicates absolute error magnitude, with values exceeding 0.25 shown in deep red.

Figure 3 illustrates the 3D reconstruction quality of the diffusion model with QSM and R2* inputs across three orthogonal planes for a representative test subject. The synthesized MPRAGE images exhibit excellent gray-white matter contrast comparable to the ground truth across both cortical and subcortical regions. Although the synthesis was performed on a slice-by-slice basis in 2D, the reconstructed 3D volume demonstrates smooth inter-slice continuity without visible discontinuities or artifacts, likely attributed to the strong spatial guidance provided by the consistent 3D anatomical structure preserved in the input mGRE sequences. This volumetric consistency is essential for downstream volumetric analysis and segmentation tasks.

Since T1w MPRAGE images are primarily acquired for anatomical segmentation in clinical practice, we evaluated the functional utility of synthesized images by assessing their performance in automated brain tissue segmentation. This analysis provides a clinically relevant measure of whether the synthesized images can preserve the anatomical information necessary for accurate morphometric analysis.

3.2 Segmentation-Based Functional Assessment

Dice Similarity Coefficient Analysis. Figure 4 presents the distribution of DSC values across eight representative brain regions for all four models evaluated on the test set ($n = 98$ subjects). Both diffusion-based models substantially outperformed the baseline methods across all regions. Notably, in the four subcortical regions where QSM and R2* information was spatially localized (caudate, pallidum, putamen, and thalamus), the incorporation of these parametric maps consistently improved segmentation accuracy. The improvements were statistically significant in the pallidum and thalamus ($p < 0.05$), regions known for their high iron content and strong susceptibility contrast. In the cerebral cortex and white matter, regions where QSM and R2* provide minimal additional information, the diffusion model with QSM/R2* showed a statistically significant

Synthetic MPRAGE Actual MPRAGE

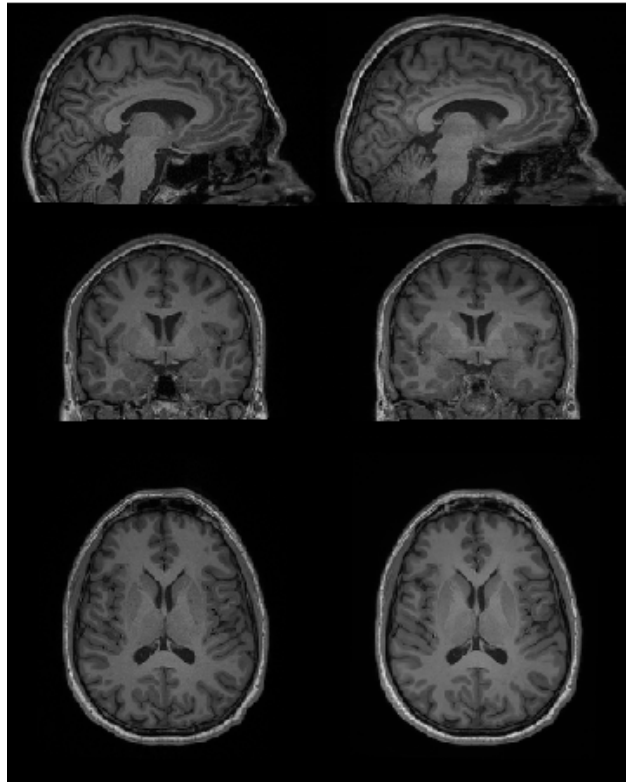


Figure 3: Representative synthesized MPRAGE images generated by the diffusion model with QSM and $R2^*$ inputs for one subject from the test set. Three orthogonal views are shown: sagittal (top row), coronal (middle row), and axial (bottom row). Left column: synthesized MPRAGE; right column: ground truth MPRAGE. The synthesized images demonstrate high-quality gray-white matter contrast in both cortical and subcortical regions. Despite being reconstructed from 2D slice-by-slice synthesis, the 3D volume exhibits smooth transitions across slices without visible discontinuities.

but clinically negligible decrease in DSC compared to the diffusion-only model (difference < 0.02), likely reflecting the increased model complexity without corresponding informational benefit in these regions. For the amygdala and hippocampus, where QSM and R2* maps were not included in the basal ganglia mask, no significant improvement was observed with the addition of these parametric inputs, as expected.

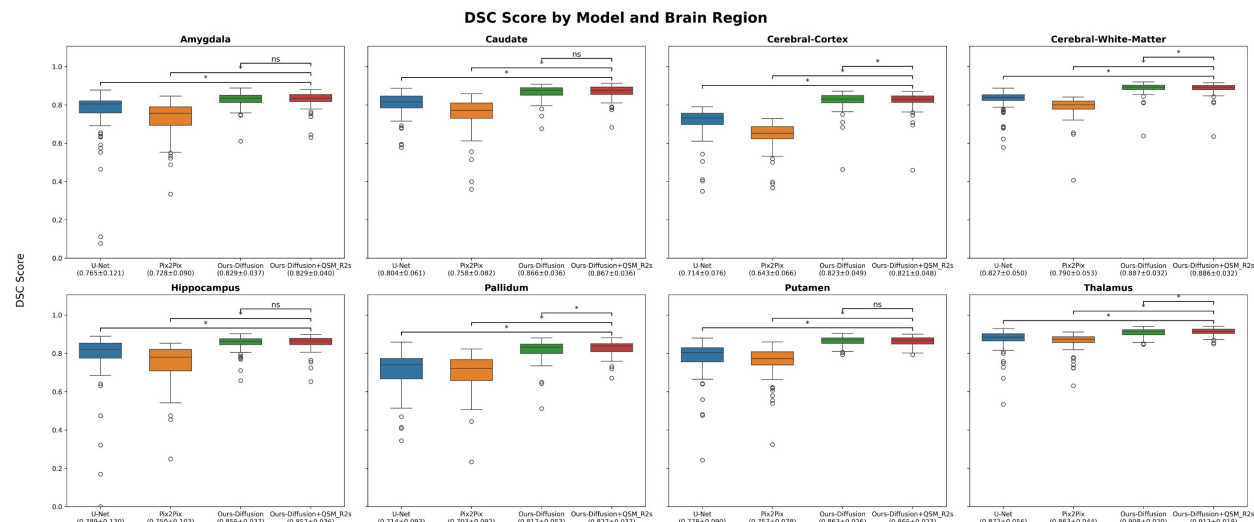


Figure 4: Segmentation accuracy comparison across eight brain regions measured by Dice Similarity Coefficient (DSC). Boxplots display DSC distributions for U-Net, Pix2Pix, our diffusion model, and our diffusion model with QSM and R2* inputs over the test set ($n = 98$ subjects). Each box represents the interquartile range (IQR), with the central line indicating the median. Whiskers extend to $1.5 \times \text{IQR}$. Statistical significance between the diffusion model and diffusion model with QSM/R2* is indicated by brackets: * denotes $p < 0.05$; ns indicates non-significant differences. Both diffusion models demonstrate superior performance compared to baseline methods across all regions.

Volumetric Reliability Analysis. To quantify the reliability of volumetric measurements derived from synthesized images, we computed the intraclass correlation coefficient (ICC2k) between model-derived and ground truth volumes for the same eight brain regions. Figure 5 shows that both diffusion models achieved substantially higher agreement with ground truth segmentations compared to baseline methods, with all ICC values exceeding the threshold of 0.75, indicating excellent reliability[34]. Consistent with the DSC results, the four subcortical regions with incorporated QSM and R2* information (caudate, pallidum, putamen, and thalamus) exhibited improved ICC scores in the diffusion model with parametric inputs compared to the diffusion-only model. In cerebral cortex and white matter, ICC values remained nearly identical between the two diffusion variants, as expected given these regions were outside the basal ganglia mask. Interestingly, for the amygdala and hippocampus, the diffusion model with QSM/R2* showed marginally higher ICC values despite these regions not receiving direct parametric input, possibly reflecting improved overall model regularization or indirect benefits from the multi-modal training.

Volumetric Accuracy Assessment. Figure 6 illustrates the median relative volumetric differences between model-derived and ground truth segmentations across all eight regions. Statistical significance was assessed using Wilcoxon signed-rank tests with Bonferroni correction ($p < 0.0025$). The results demonstrate that diffusion models achieved significantly better volumetric accuracy compared to baseline methods. Both diffusion models produced volumes that were nearly identical to ground truth measurements in most regions, although all four models exhibited statistically significant differences in cortical volume estimates, likely reflecting the inherent challenges in accurately delineating the highly convoluted cortical ribbon. Nevertheless, even in the cortex, diffusion models substantially outperformed baselines, with median relative differences approaching zero. The two diffusion model variants produced highly comparable volumetric estimates across all regions, with differences between them being minimal and clinically negligible.

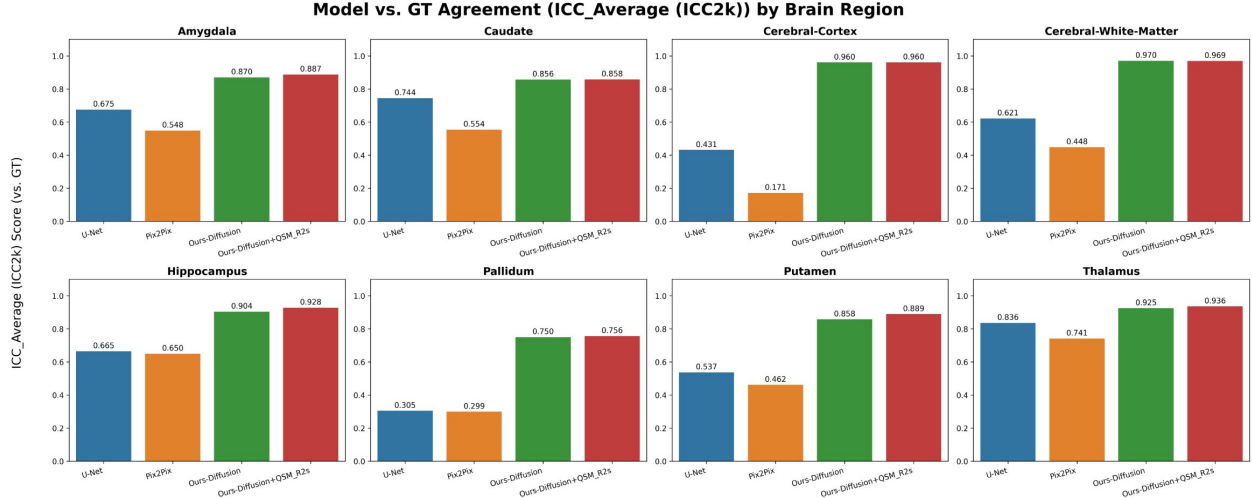


Figure 5: Volumetric measurement reliability assessed by intraclass correlation coefficient (ICC2k) across eight brain regions. Bar plots compare ICC values for U-Net, Pix2Pix, diffusion model, and diffusion model with QSM and R2* inputs. Both diffusion-based models achieve substantially higher agreement with ground truth MPRAGE-derived volumes compared to baseline methods, with the addition of QSM and R2* providing comparable or improved consistency, particularly in subcortical regions with high iron content.

3.3 Biological Plausibility Assessment

To validate whether the synthesized images preserve the biological dependencies found in real populations, we performed multiple linear regression analyses on nine ROIs. Table 2 presents the comparison of regression statistics between ground truth (D_{GT}) and data synthesized by our proposed diffusion model with multi-parametric integration (D_{GEN}).

Ageing Effects. As expected in a healthy aging population, the ground truth data exhibited widespread age-related atrophy, indicated by negative regression coefficients (β_{Age}) across most regions. Crucially, the synthesized data (D_{GEN}) accurately replicated these trends. For instance, in the *Thalamus*, a region known to be sensitive to aging, the generated data showed a regression coefficient of $\beta_{Age} = -48.51$ ($p < 0.001$), which is highly consistent with the ground truth ($\beta_{Age} = -51.36$). Furthermore, the effect sizes of aging, measured by Cohen’s f , showed remarkable alignment between datasets (e.g., *Thalamus*: $f_{GEN} = 0.6766$ vs. $f_{GT} = 0.8271$; *Cerebral Cortex*: $f_{GEN} = 1.0118$ vs. $f_{GT} = 1.2038$). This suggests that our generative model successfully captures the subtle, non-linear morphological changes associated with aging.

Sex Differences. Regarding sexual dimorphism, the synthesized data preserved the general patterns of sex-related differences observed in the real data. The Cohen’s d values generally aligned with the ground truth categories across most ROIs. Crucially, for regions with negligible or small sex effects (e.g., *Caudate* and *Pallidum*), the generative model correctly identified them as having lower sexual dimorphism ($d_{GEN} < 0.5$) compared to highly dimorphic regions like the *Thalamus* and *Amygdala*. Although minor variations in effect size magnitudes were observed in these low-contrast regions (e.g., *Pallidum*), the model successfully retained the overall biological hierarchy of sex differentiation.

Overall Model Fit. The adjusted R^2 values, which quantify the proportion of variance explained by the demographic variables, were highly comparable between D_{GT} and D_{GEN} . This similarity indicates that the synthesized images do not introduce varying levels of noise that would obscure biological signals.

In summary, the high concordance of β_{Age} , Cohen’s f , and Cohen’s d between the two groups demonstrates that our diffusion-based method generates strictly biologically plausible images, making them suitable for downstream clinical analysis.

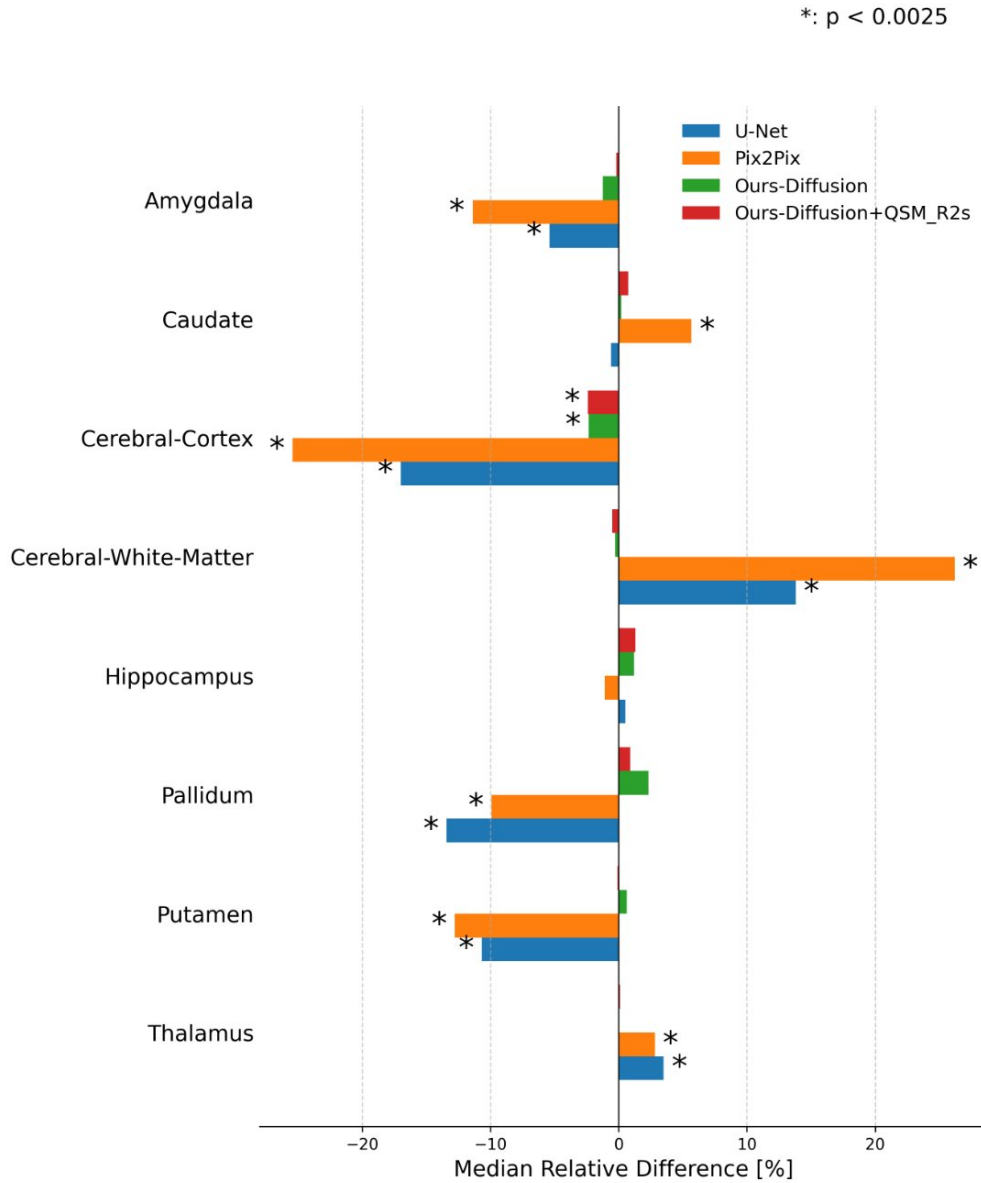


Figure 6: Median relative volumetric differences compared to ground truth across eight brain regions. Boxplots show the distribution of relative volume errors (computed as $\frac{V_{\text{model}} - V_{\text{GT}}}{V_{\text{GT}}} \times 100$) for each model. The horizontal dashed line at 0 indicates perfect agreement. Statistical significance is indicated by asterisks (: p < 0.0025 after Bonferroni correction). Both diffusion models demonstrate superior volumetric accuracy with median differences close to zero in most regions, substantially outperforming U-Net and Pix2Pix baselines.

Table 2: Comparison of regression statistics between ground truth (D_{GT}) and generated (D_{GEN}) data across nine ROIs. The metrics include adjusted R^2 , regression coefficient for age (β_{Age}), Cohen’s f for aging effect size, regression coefficient for sex (β_{Sex}), and Cohen’s d for sex effect size. Note that volumetric ROIs are measured in mm^3 , and cortical thickness is measured in mm.

ROI	Source	Adj. R^2	Age Effect			Sex Effect		
			β_{Age}	p_{Age}	f_{Age}	β_{Sex}	p_{Sex}	d_{Sex}
Amygdala	GT	0.2679	-6.182	7.89×10^{-4}	0.3579	309.2	5.21×10^{-4}	0.7413
	GEN	0.2477	-5.781	0.0016	0.3361	220.7	0.0104	0.5391
Caudate	GT	0.2561	-12.81	0.0031	0.3137	6.314	0.9753	0.0064
	GEN	0.3331	-9.946	0.0103	0.2701	116.9	0.5194	0.1334
Hippocampus	GT	0.3999	-14.66	4.15×10^{-5}	0.4436	486.1	0.0040	0.6093
	GEN	0.4695	-11.81	7.25×10^{-4}	0.3605	531.3	0.0013	0.6817
Pallidum	GT	0.3946	-7.836	8.83×10^{-5}	0.4227	83.97	0.3655	0.1876
	GEN	0.2483	-5.639	0.0171	0.2505	249.3	0.0264	0.4655
Putamen	GT	0.5536	-29.02	3.68×10^{-11}	0.7726	424.1	0.0257	0.4676
	GEN	0.4641	-24.79	4.16×10^{-7}	0.5614	395.2	0.0715	0.3761
Thalamus	GT	0.6234	-51.36	2.91×10^{-12}	0.8271	1270	8.59×10^{-5}	0.8469
	GEN	0.5199	-48.51	2.90×10^{-9}	0.6766	933.3	0.0094	0.5471
Cerebral Cortex	GT	0.8008	-1293	5.52×10^{-20}	1.2038	16650	0.0025	0.6419
	GEN	0.8169	-986.4	4.66×10^{-16}	1.0118	17110	5.53×10^{-4}	0.7376
Cerebral White Matter	GT	0.6543	-616.9	3.39×10^{-4}	0.3836	15240	0.0601	0.3926
	GEN	0.6630	-560.5	6.32×10^{-4}	0.3648	11380	0.1346	0.3113
Mean Cortical Thickness	GT	0.3771	-0.0030	9.44×10^{-12}	0.7966	-0.0074	0.6584	-0.0910
	GEN	0.3663	-0.0019	2.57×10^{-11}	0.7752	-0.0011	0.9182	-0.0211

4 Conclusion

In this study, we presented a multi-parametric MRI synthesis framework based on the Fast-DDPM architecture to generate high-contrast 3D T1w MPRAGE images directly from multi-echo GRE sequences. By extending the diffusion model to integrate iron-sensitive QSM and R2* maps as conditional inputs, our method effectively addresses the challenge of contrast ambiguity in iron-rich deep gray matter structures, which is a common limitation in conventional intensity-based synthesis.

Our comprehensive evaluation demonstrates that the proposed framework significantly outperforms established U-Net and GAN-based baselines in both perceptual image quality and volumetric segmentation accuracy. Crucially, beyond pixel-level metrics, we validated the biological plausibility of the synthesized images through rigorous statistical analysis. The high concordance of aging effects (β_{Age} , Cohen's f) and sexual dimorphism patterns (Cohen's d) between the synthesized and ground truth data confirms that our generative model preserves essential population-level morphological dependencies. This indicates that the synthesized T1w images are reliable for downstream morphometric analyses.

Clinically, our approach offers a promising pathway to streamline neuroimaging protocols by eliminating the need for separate T1w acquisitions when mGRE data is available, potentially reducing scan time and patient burden. Future work will focus on extending this framework to fully 3D architectures to better capture global anatomical context, validating the model's generalizability on multi-center datasets, and exploring its applicability in detecting pathological atrophy in neurodegenerative diseases.

References

- [1] John P Mugler and James R Brookeman. Three-dimensional magnetization-prepared rapid gradient-echo imaging (3d mp rage). *Magnetic Resonance in Medicine*, 15(1):152–157, 1990.
- [2] Martin Reuter, Nicholas J Schmansky, H Diana Rosas, and Bruce Fischl. Within-subject template estimation for unbiased longitudinal image analysis. *NeuroImage*, 61(4):1402–1418, 2012.
- [3] Juliana HR O Barbosa, Antônio Carlos Santos, Vitor Tumas, Min Liu, Weiwei Zheng, E Mark Haacke, and Carlos EG Salmon. Quantifying brain iron deposition in patients with parkinson's disease using quantitative susceptibility mapping, r2 and r2*. *Magnetic Resonance Imaging*, 33(5):559–565, 2015.
- [4] Chunlei Liu, Wei Li, Karen A Tong, Kristen W Yeom, and Samuel Kuzminski. Quantitative susceptibility mapping: Contrast mechanisms and clinical applications. *Tomography*, 1(1):3–17, 2015.
- [5] Tonghe Wang et al. A review on medical imaging synthesis using deep learning and its clinical applications. *Journal of Applied Clinical Medical Physics*, 22(1):11–36, 2021.
- [6] Amirhossein Kazerouni, Ehsan Khodapanah Aghdam, Moein Heidari, et al. Diffusion models in medical imaging: A comprehensive survey. *Medical Image Analysis*, 88:102846, 2023.
- [7] Eileen Johnstone, Jonathan J Wyatt, Ann M Henry, et al. Systematic review of synthetic computed tomography generation methodologies for use in magnetic resonance imaging-only radiation therapy. *International Journal of Radiation Oncology* Biology* Physics*, 100(1):199–217, 2018.
- [8] Snehashis Roy, Amod Jog, Aaron Carass, and Jerry L Prince. Atlas based intensity transformation of brain mr images. In *Multimodal Brain Image Analysis*, pages 51–62. Springer, 2013.
- [9] Olaf Ronneberger, Philipp Fischer, and Thomas Brox. U-net: Convolutional networks for biomedical image segmentation. In *Medical Image Computing and Computer-Assisted Intervention–MICCAI 2015*, pages 234–241. Springer, 2015.

- [10] Xiao Han. Mr-based synthetic ct generation using a deep convolutional neural network method. *Medical Physics*, 44(4):1408–1419, 2017.
- [11] Ian Goodfellow, Jean Pouget-Abadie, Mehdi Mirza, et al. Generative adversarial nets. In *Advances in Neural Information Processing Systems*, volume 27, pages 2672–2680, 2014.
- [12] Phillip Isola, Jun-Yan Zhu, Tinghui Zhou, and Alexei A Efros. Image-to-image translation with conditional adversarial networks. In *Proceedings of the IEEE Conference on Computer Vision and Pattern Recognition*, pages 1125–1134, 2017.
- [13] Youssef Skandarani, Pierre-Marc Jodoin, and Alain Lalonde. Gans for medical image synthesis: An empirical study. *Journal of Imaging*, 9(3):69, 2023.
- [14] Jonathan Ho, Ajay Jain, and Pieter Abbeel. Denoising diffusion probabilistic models. In *Advances in Neural Information Processing Systems*, volume 33, pages 6840–6851, 2020.
- [15] Yiqing Shi, Gaofeng Huang, Yonghong Wang, et al. Diffusion models for medical image computing: A survey. *Tsinghua Science and Technology*, 30(1):357–383, 2025.
- [16] Lan Jiang, Chenyu Yan, Jian Zhang, et al. Cola-diff: Conditional latent diffusion model for multi-modal mri synthesis. In *Medical Image Computing and Computer Assisted Intervention–MICCAI 2023*, volume 14229, pages 398–408. Springer, 2023.
- [17] Firas Khader, Gustav Mueller-Franzes, Soroosh Tayebi Arasteh, et al. Denoising diffusion probabilistic models for 3d medical image generation. *Scientific Reports*, 13(1):7303, 2023.
- [18] Hongxiang Jiang, Imran Muhammad, Teng Zhang, Yuyin Zhou, Muxuan Liang, Kuang Gong, and Wei Shao. Fast-ddpm: Fast denoising diffusion probabilistic models for medical image-to-image generation. *IEEE Journal of Biomedical and Health Informatics*, 29(1):1–11, 2025.
- [19] Christian Langkammer, Ferdinand Schweser, Nicole Krebs, et al. Quantitative susceptibility mapping (qsm) as a means to measure brain iron? a post mortem validation study. *NeuroImage*, 62(3):1593–1599, 2012.
- [20] Julio Acosta-Cabronero, Matthew J Betts, Arturo Cardenas-Blanco, Shuang Yang, and Peter J Nestor. In vivo mri mapping of brain iron deposition across the adult lifespan. *Journal of Neuroscience*, 36(2): 364–374, 2016.
- [21] Julien Cohen-Adad. What can we learn from t_2^* maps of the cortex? *NeuroImage*, 93:189–200, 2014.
- [22] Kanghyun Ryu, Na-Young Shin, Dong-Hyun Kim, and Yoonho Nam. Synthesizing t_1 weighted mprage image from multi echo gre images via deep neural network. *Magnetic Resonance Imaging*, 64:13–20, 2019.
- [23] D Qiu, G. C.-F. Chan, J Chu, and et al. Mr quantitative susceptibility imaging for the evaluation of iron loading in the brains of patients with β -thalassemia major. *American Journal of Neuroradiology*, 35(6): 1085–1090, 2014.
- [24] Qixiang Lin, Junjie Wu, Shuai Huang, et al. Brain iron deposition in healthy aging and association with alzheimer’s disease pathology revealed by quantitative susceptibility mapping. *Proc. Intl. Soc. Mag. Reson. Med.*, 30:4035, 2022.

- [25] Qixiang Lin, Salman Shahid, Antoine Hone-Blanchet, et al. Magnetic resonance evidence of increased iron content in subcortical brain regions in asymptomatic alzheimer’s disease. *Human Brain Mapping*, 44(8):3072–3083, 2023.
- [26] Mark Jenkinson, Christian F. Beckmann, Timothy E. J. Behrens, et al. Fsl. *NeuroImage*, 62(2):782–790, 2012. ISSN 1053-8119. doi: 10.1016/j.neuroimage.2011.09.015.
- [27] B Hallgren and P Sourander. The effect of age on the non-haemin iron in the human brain. *Journal of Neurochemistry*, 3(1):41–51, 1958. doi: 10.1111/j.1471-4159.1958.tb12607.x.
- [28] David J Madden, Jenna L Merenstein, et al. Quantitative susceptibility mapping of brain iron in healthy aging and cognition. *NeuroImage*, 282:120401, 2023. doi: 10.1016/j.neuroimage.2023.120401.
- [29] C Ghadery, L Pirpamer, E Hofer, et al. R2* mapping for brain iron: associations with cognition in normal aging. *Neurobiology of Aging*, 36(3):925–932, 2015. doi: 10.1016/j.neurobiolaging.2014.09.013.
- [30] Diederik P. Kingma and Jimmy Ba. Adam: A method for stochastic optimization. *arXiv preprint arXiv:1412.6980*, 2014.
- [31] Zhou Wang, Alan Conrad Bovik, Hamid Rahim Sheikh, et al. Image quality assessment: From error visibility to structural similarity. *IEEE Transactions on Image Processing*, 13(4):600–612, 2004.
- [32] Kelly H. Zou, Simon K. Warfield, Ajit Bharatha, et al. Statistical validation of image segmentation quality based on a spatial overlap index. *Academic Radiology*, 11(2):178–189, 2004.
- [33] Patrick E. Shrout and Joseph L. Fleiss. Intraclass correlations: Uses in assessing rater reliability. *Psychological Bulletin*, 86(2):420–428, 1979.
- [34] Terry K. Koo and Mae Y. Li. A guideline of selecting and reporting intraclass correlation coefficients for reliability research. *Journal of Chiropractic Medicine*, 15(2):155–163, 2016.
- [35] Randy L. Buckner, Denise Head, Jennifer Parker, et al. A unified approach for morphometric and functional data analysis in young, old, and demented adults using automated atlas-based head size normalization. *NeuroImage*, 23(2):724–738, 2004.
- [36] Jacob Cohen. *Statistical Power Analysis for the Behavioral Sciences*. Lawrence Erlbaum Associates, Hillsdale, NJ, 2nd edition, 1988. ISBN 978-0-8058-0283-2.